

A new approach to roughness-induced vibrations on a slider

Janko Slavič^{a,b,*}, Michael D. Bryant^b, Miha Boltežar^a

^aUniversity of Ljubljana, Faculty of Mechanical Engineering, Aškerčeva 6, 1000 Ljubljana, Slovenia

^bUniversity of Texas at Austin, Mechanical Engineering Department, Austin, TX 78712-1063, USA

Received 27 September 2006; received in revised form 19 June 2007; accepted 19 June 2007

Abstract

In the past, roughness effects were included in models by using various friction laws. In contrast, this study deals with simple Poisson impact and Coulomb friction laws on multiple concurrent contacts between geometrically random rough surfaces and their effect on the slider's roughness-induced vibrations.

The closed-form solutions derived here relate roughness-induced vibrations to the surface roughness, slider mass, slider load, slider dimensions, relative sliding speed, and the coefficient of restitution. Wear influences were studied by simulating random rough surfaces with multiple concurrent contacts.

Contrary to expectations we found that random roughness can induce slider vibrations of distinct frequencies. We found a good agreement between the results of the studied models and the experiments.

The closed-form solution was found to be suitable for estimating the roughness-induced vibration frequencies of a hard-disk drive's writing/reading head and those of a car-brake's pad (known as squeal-noise).

© 2007 Elsevier Ltd. All rights reserved.

1. Introduction

Sliding contacts with friction can induce vibrations via mechanisms of stick–slip, variable dynamic-friction coefficient, sprag-slip, and coupling mechanisms [1–5]. Using a simplified model of orthogonal cutting, Grabec [6] showed that besides limit-cycle vibrations, dry friction can produce chaotic motions. Popp and Stelter [7], Ibrahim [5], and others overviewed stick–slip vibrations and chaos.

Impacts are sources of self-sustained oscillations or chaotic motion. Whiston [8] investigated the steady-state response of a single-degree-of-freedom (dof) oscillator under harmonic excitation. Shaw and Holmes [9] showed that even a single-dof impact oscillator can produce harmonic, subharmonic and chaotic motions. Impact oscillators have been studied for governing equations [10,11], for relatively simple mechanical models [12] and for real-life applications (e.g., gear rattle by Pfeiffer and Kunert [13]). Bishop [14] overviews impacting oscillators.

Contact models between rigid bodies for dry-friction only, impacts only, or dry-friction and impacts usually involve point contacts, for tractable solutions. Consequently, parametric studies give undue emphasis to different friction laws, the number of degrees of freedom [15,16], vibro-isolation, and harmonic excitations,

*Corresponding author. University of Ljubljana, Faculty of Mechanical Engineering, Aškerčeva 6, 1000 Ljubljana, Slovenia.
Tel.: +386 1 4771 200; fax: +386 1 2518 567.

E-mail address: janko.slavic@fs.uni-lj.si (J. Slavič).

Nomenclature			
<i>Indices</i>		l	slider height
		\mathbf{M}	mass matrix
		m	slider mass
C	end of compression phase or compression phase	p	number of concurrent contacts
E	end of expansion phase or expansion phase	\mathbf{q}	generalized coordinates
S	start of compression phase	r	contact point distance
n	normal direction	T	time between two impacts
t	tangential direction	T_{sim}	simulated time
<i>Variables</i>		u	wear of surface height
		v_v	vertical velocity
		v_s	horizontal velocity
		W_i	loss of mechanical energy at contact point i
F	slider load	\mathbf{W}	constraint matrix of contacts
f_b	frequency of bouncing	w	slider width
f_c	closed-form frequency of bouncing with rocking	w_g	counter surface width
f_m	measured frequency	\mathbf{w}	constraint vector of contact
\dot{g}	relative sliding speed	X	Fourier transform of x
h	height of bouncing	x	translational degree of freedom
\mathbf{h}	vector of active forces	α	change of slope between asperities
I	total impulse (compression+expansion)	ζ	angle sawtooth slope
J	slider mass moment of inertia	ε	coefficient of restitution
K_ε	influence of ε on vibrations	μ	coefficient of friction
K_{lr}	influence of slider shape on vibrations	Φ	Fourier transform of φ
k_l	ratio of slider height l to width w	φ	rotational degree of freedom
k_r	ratio of contact distance r to slider width w	σ_α	standard deviation of angle α

among others, while overlooking other influences. By applying different variations of Coulomb's friction law, stick–slip phenomena can be studied [17]. Via an acceleration-dependent friction-law, McMillan [18] found that the initial conditions are important in stick–slip phenomena. Vielsack [19] studied four different friction laws and found that the stick–slip during deceleration depends on the properties of the mechanical system, especially the drive, and less on the characteristics of the frictional force. Ogilvy [20] and later Bengisu and Akay [21] studied the relation between dry friction and surface roughness. Ono and Iida [22] used a single-dof, single-contact model for a statistical analysis of random roughness on vibration amplitudes. Roughness effects on impact properties were studied by Chang and Ling [23]. In addition, the coupling of normal and tangential vibrations can lead to stick–slip phenomena [24,25]. Parametric resonances analyzed by Mottershead et al. [26] can also lead to increased vibrations.

This article studies the influence of random roughness and run-in wear on slider vibrations. The results for theoretical and experimental investigation are presented. The slider dynamics was analyzed with simple closed-form analytical models and more complex numerical models. In Section 2, a simple steady-state bouncing model involving a single contact is developed. Section 3 develops a two-contact steady-state bouncing-with-rocking model, which includes surface roughness, slider mass, slider load, slider dimensions, relative sliding speed, and the coefficient of restitution. Section 4 introduces numerical models with one and two contacts and progresses to a multiple-contact model between rough surfaces. Run-in wear is also presented. A comparison and discussion of analytical and numerical models are given in Section 5. Section 6 presents experiments to verify the models and also compares the results to published experiments on hard-disk drives and brakes. Section 7 presents a summary with conclusions.

2. Steady-state bouncing

Paddle juggling, i.e., repeatedly hitting a ball attached by an elastic cord to a paddle, exhibits steady-state bouncing. By hitting the ball vertically with a flat horizontal paddle, the ball is kept in the air. The ball exhibits periodic motion, motion that stays on a strange attractor, and chaotic motion dependent on the frequency and amplitude of the oscillation of the paddle [27–29]. Wood and Byrne [27] studied the bouncing of a ball on a randomly vibrating surface. The variation of the oscillating horizontal paddle, with a constant downward force F acting on the ball, is shown in Fig. 1a. During contact the sawtooth-shaped counter-surface—moving horizontally with velocity v_s —impacts and applies the vertical velocity

$$v_v = v_s \tan \xi \tag{1}$$

to the ball of mass m , where ξ is the sawtooth slope, see Fig. 1b. By neglecting the effects on the dynamics of the ball’s radius, sawtooth height, and assuming that the counter surface mass is infinite, the simplified model in Fig. 1c applies. Here, the rigid ball always touches the rigid sawtooth at the same height with a vertical velocity v_v .

For rigid bodies Poisson’s law for elastic collision solves the impacts as a compression phase with diminishing relative normal velocities, followed by an expansion phase [30]. With Poisson’s law, the expansion-phase impulse $I_E = \varepsilon I_C$, where I_C is the compression impulse. The total impulse $I = I_C + I_E$, the time integral of force, is usually related to the momentum difference before and after an impact. The coefficient of restitution, ε , is in the range [0,1], where 0 denotes plastic and 1 perfectly elastic impacts. Common assumptions for impact include a short duration for the impacts, unchanged positions of the bodies, and negligible non-impulsive forces (moderate forces of long duration).

The subscripts S , C , and E denote the start of compression, the end of the compression, and the end of the expansion phase, respectively. For example, \dot{x}_S and \dot{x}_E denote the velocities at the start of the compression and the end of the expansion, respectively. The expansion phase starts at C , the end of the expansion.

The compression impulse $I_C = m(v_v - \dot{x}_S)$ is followed by the expansion impulse $I_E = \varepsilon I_C$:

$$I = I_C + I_E = m(v_v - \dot{x}_S) + \varepsilon m(v_v - \dot{x}_S). \tag{2}$$

Relating the impulse I to the momentum difference between the start and the finish, $m\dot{x}_E - m\dot{x}_S$, of an impact gives

$$\dot{x}_E = -\varepsilon\dot{x}_S + v_v(1 + \varepsilon), \tag{3}$$

where \dot{x}_S is the pre-impact velocity. We are interested in sustained period-one motion, which means that the ball must always touch the sawtooth surface at the same height, h , and obey the condition $\dot{x}_E = -\dot{x}_S$. The displacement x and the velocity \dot{x} versus time for a sustainable periodic motion are plotted in Fig. 1d, which is a result of solving Newton’s law $m\ddot{x} = -F$ between impacts, with the initial conditions $x(0) = 0$ and $\dot{x}(0) = \dot{x}_E$. Combining $\dot{x}_E = -\dot{x}_S$ and Eq. (3) gives

$$\dot{x}_E = v_v K_\varepsilon^{-1}, \tag{4}$$

where

$$K_\varepsilon = \frac{1 - \varepsilon}{1 + \varepsilon} \tag{5}$$

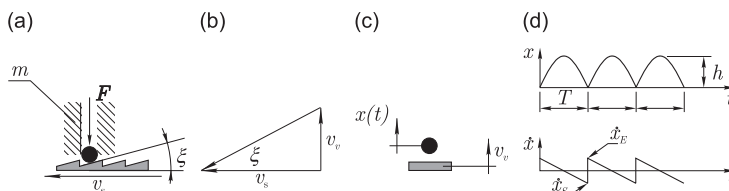


Fig. 1. 1-dof Ball bouncing against sawtooth surface: (a) model, (b) vertical velocity, (c) impact model, (d) steady-state bouncing.

monotonically decreases from 1 to 0 for a coefficient of restitution, ϵ , between 0 and 1, respectively. The impulse on the ball during the collision is

$$I = I_C + I_E = 2\dot{x}_E m. \tag{6}$$

From the conservation of kinetic and potential energies between any two impacts, the height of the bounce (see Fig. 1d) is

$$h = \frac{m\dot{x}_E^2}{2F}. \tag{7}$$

A constant force F applied over a period T renders the total impulse $I = FT$. From the conservation of linear momentum, the frequency f_b and the period T of the periodic bouncing are

$$f_b = \frac{1}{T} = \frac{F}{I} = \frac{F}{2mv_v} K_\epsilon. \tag{8}$$

3. Steady-state bouncing-with-rocking of a slider

Fig. 2 depicts a two-degrees-of-freedom rigid slider, free to translate in the vertical x direction and rotate about the angle φ . The slider has width w , length l , mass m , and so the mass moment of inertia $J = m(w^2 + l^2)/12$. The right (R) and left (L) contact points between the slider and the counter surface are defined by the distance r from the centre of mass of the slider, and the value of φ at the impact. It is assumed that there is no friction between the slider and the counter surface. Although the counter surface is not moving vertically at the moment of impact, the counter surface is assumed to apply a vertical velocity v_v to the slider via a roughness-effect coupling similar to the sawtooth surface of Fig. 1.

With a constant vertical force, F , applied to the centre of mass of the slider, the equations of motion during the non-contact state are:

$$m\ddot{x} = -F, \tag{9}$$

$$J\ddot{\varphi} = 0. \tag{10}$$

Assuming a slider that is symmetrical about its centre of mass, the response needs to be analyzed at only one contact point (e.g., the left). As in the ball bouncing of Section 2, Poisson’s law governs the bouncing with rocking, and S , C , and E denote the start of the compression, the end of the compression, and the end of the expansion. In Fig. 2, $I_n = I_{nC} + I_{nE}$ and $I_t = I_{tC} + I_{tE}$ denote the total impact impulse on the slider, as the sum of the compression and the expansion impulses. The subscripts n and t refer to the normal and tangential directions.

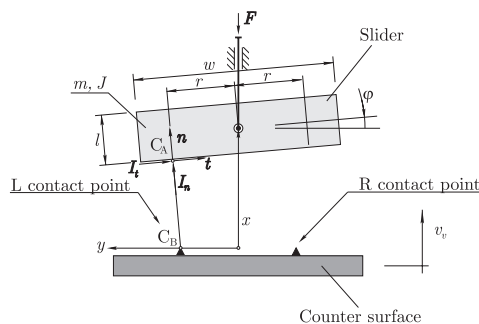


Fig. 2. 2-dof Model with Left and Right contact points.

3.1. Compression phase

Without friction, only the normal compression impulse I_{nC} is active (see I_n in Fig. 2). With Poisson's law the non-impact forces are assumed to be negligible. The conservation of momentum for the bouncing slider gives

$$I_{nC} \cos \varphi_C = m\dot{x}_C - m\dot{x}_S, \quad (11)$$

$$-rI_{nC} = J\dot{\varphi}_C - J\dot{\varphi}_S, \quad (12)$$

where the slider velocities at the start and the end of the compression phase are \dot{x}_S , $\dot{\varphi}_S$ and \dot{x}_C , $\dot{\varphi}_C$, respectively. To determine the normal compression impulse, I_{nC} , as a function of the velocities at S , eliminate the velocities at C using the condition that at the end of the compression the relative normal velocity is zero. The relative velocity vector between the bodies at the end of the compression (in the coordinate system $x - y$, Fig. 2) is

$$\begin{aligned} \dot{\mathbf{r}}_C &= \dot{\mathbf{r}}_{CA} - \dot{\mathbf{r}}_{CB} \\ &= \begin{pmatrix} \dot{x}_C - r\dot{\varphi}_C \cos \varphi_C + l/2\dot{\varphi}_C \sin \varphi_C - v_v \\ -r\dot{\varphi}_C \sin \varphi_C - l/2\dot{\varphi}_C \cos \varphi_C \end{pmatrix}^T, \end{aligned} \quad (13)$$

where A and B denote the slider and the counter surface and T denotes the matrix transpose. In the $n - t$ coordinate system, shown at the bottom of the slider in Fig. 2, the relative normal velocity

$$\dot{g}_{nC} = \mathbf{n}_C^T \cdot \dot{\mathbf{r}}_C = -v_v \cos \varphi_C + \dot{x}_C \cos \varphi_C - r\dot{\varphi}_C = 0 \quad (14)$$

at the end of the compression must vanish, where the unit normal vector $\mathbf{n}_C = (\cos \varphi_C, \sin \varphi_C)^T$.

The normal compression-impulse, I_{nC} , is found by eliminating \dot{x}_C and $\dot{\varphi}_C$ from Eqs. (11), (12), and (14), giving

$$I_{nC} = -\frac{Jm\dot{g}_{nS}}{mr^2 + J \cos^2 \varphi_S}, \quad (15)$$

where

$$\dot{g}_{nS} = \mathbf{n}_{A,S}^T \dot{\mathbf{r}}_S = -v_v \cos \varphi_S + \dot{x}_S \cos \varphi_S - r\dot{\varphi}_S. \quad (16)$$

Eqs. (15) and (16) assume $\varphi_S = \varphi_C$, consistent with Poisson's law's assumptions about the short time of the impact (which allows the displacements to be considered as constant).

3.2. Expansion phase

The expansion-phase impulse $I_{nE} = \varepsilon I_{nC}$ follows the compression phase. The total impulse during the impact $I = I_{nC} + I_{nE} = (1 + \varepsilon)I_{nC}$.

3.3. Steady-state response

Similar to Eqs. (11) and (12), the conservation of linear and angular momentum during the overall impact (compression plus expansion) gives

$$(1 + \varepsilon)I_{nC} \cos \varphi_C = m\dot{x}_E - m\dot{x}_S, \quad (17)$$

$$-r(1 + \varepsilon)I_{nC} = J\dot{\varphi}_E - J\dot{\varphi}_S. \quad (18)$$

From the motion equation (9), the conservation of linear momentum between the left (L) and right (R) impacts gives

$$m\dot{x}_E^L - FT = m\dot{x}_S^R, \quad (19)$$

where T is the period between the L and R impacts and F is a constant. The subscripts in Eq. (19) indicate at which instant during the impact the velocity was evaluated. A constant angular momentum between the L and

R impacts (no external moments on the slider between the impacts) and $\varphi_E^L = \varphi_E^R = \varphi_E$ give

$$\dot{\varphi}_E T + 2\varphi_E = 0. \tag{20}$$

For a sustainable steady-state bouncing, the one-contact model condition $\dot{x}_E = -\dot{x}_S$ is enhanced with the rocking condition $\dot{\varphi}_E = -\dot{\varphi}_S$. Substituting these conditions into Eqs. (17) to (20), enforcing Poisson’s constant-displacement assumption during impact, and eliminating T , \dot{x}_E , and $\dot{\varphi}_E$ gives

$$F(\varepsilon - 1)^2 \varphi_E = \frac{Jm^2rv_v^2(\varepsilon + 1)^2 \cos^3(\varphi_E)}{(mr^2 + J \cos^2(\varphi_E))^2}. \tag{21}$$

Using a small-angle approximation, $\cos \varphi_E \approx 1$, with $J = m(w^2 + l^2)/12$ and the normalizations $k_r = r/w$, and $k_l = l/w$, Eq. (21) leads to

$$\varphi_E = \frac{12mv_v^2}{Fw} \frac{k_r}{1 + k_l^2} K^2. \tag{22}$$

In the foregoing $K = -K_{lr}^{-1}K_\varepsilon^{-1}$, where K_ε is given by Eq. (5) and

$$K_{lr}^{-1} = \frac{1 + k_l^2}{1 + k_l^2 + 12k_r^2}. \tag{23}$$

From Eqs. (17) to (20) with a small-angle approximation the velocities after impact are

$$\dot{x}_E = \sqrt{\frac{FJ\varphi_E}{m^2r}} = v_v|K|, \tag{24}$$

$$\dot{\varphi}_E = -\frac{F\varphi_E}{m\dot{x}_E} = -\frac{12v_v}{w} \frac{k_r}{1 + k_l^2} |K|. \tag{25}$$

The frequency of the bouncing-with-rocking from Eq. (19) and $\dot{x}_E = -\dot{x}_S$ is

$$f = \frac{1}{T} = \frac{F}{2m\dot{x}_E} = \frac{F}{2mv_v|K|}. \tag{26}$$

When r diminishes or l becomes large, $K_{lr} \rightarrow 1$, Eq. (23) gives $K \rightarrow -K_\varepsilon^{-1}$. A limiting situation resulting in pure bouncing similar to Eq. (8) occurs with the frequency

$$f_b = \lim_{k_r \rightarrow 0} f = \lim_{k_l \rightarrow \infty} f = \frac{F}{2mv_v} K_\varepsilon. \tag{27}$$

Using Eq. (27) the frequency of the bouncing-with-rocking is

$$f_c = f_b K_{lr}. \tag{28}$$

The parameter K_{lr} describes how the bouncing-with-rocking oscillations differ from pure bouncing oscillations. Depending on the relative dimensions k_l and k_r , K_{lr} ranges from 1 to 4. Eq. (28), however, suggests higher frequencies for bouncing with rocking, and this result is independent of the slider width, w .

4. Bouncing-with-rocking numerical simulations

The bouncing model depicted in Fig. 2 uses an idealized impact condition to estimate the vertical velocity v_v applied to the slider at the contact. If the sawtooth model is used instead, the symmetry between left and right is disturbed, and a closed-form solution is likely to be intractable. In this section a two-contact non-symmetrical numerical model with a sawtooth-shaped counter surface having the sawtooth angle ξ will be presented.

4.1. Multibody dynamics formulation

For the bouncing contact of Fig. 3, because of the sawtooth-shaped surface, the locus of the contact points cannot be specified *a priori*. The numerical methods used in this article, common in the field of multibody dynamics, have been tested and verified on classical problems [31–33].

The equations of motion in matrix form are

$$\mathbf{M}\ddot{\mathbf{q}} - \mathbf{h} = \mathbf{0}, \tag{29}$$

with the generalized coordinates $\mathbf{q} = (x, \varphi)^T$, the generalized active forces $\mathbf{h} = (-F, 0)^T$, and the mass matrix

$$\mathbf{M} = \begin{pmatrix} m & 0 \\ 0 & J \end{pmatrix}. \tag{30}$$

4.1.1. Compression phase

Similar to Eqs. (11) and (12), the conservation of momentum during the compression for p concurrent contacts gives

$$\mathbf{M}(\dot{\mathbf{q}}_C - \dot{\mathbf{q}}_S) - (\mathbf{W}_n \ \mathbf{W}_t) \begin{pmatrix} \mathbf{I}_{nC} \\ \mathbf{I}_{tC} \end{pmatrix} = \mathbf{0}. \tag{31}$$

Here, the vectors \mathbf{I}_{nC} and \mathbf{I}_{tC} of dimension p are compression impulses (in the normal and tangential directions), and the constraint matrix $(\mathbf{W}_n \ \mathbf{W}_t)$ transforms from the local $n - t$ coordinates to the generalized space. For the normal direction, the sub-matrix is

$$\mathbf{W}_n = \{\mathbf{w}_{n,1}, \mathbf{w}_{n,2}, \dots, \mathbf{w}_{n,p}\}, \tag{32}$$

where

$$\mathbf{w}_{n,i} = \left(\frac{\partial \dot{\mathbf{r}}_{C,i}}{\partial \dot{\mathbf{q}}} \right)^T \cdot \mathbf{n}_i. \tag{33}$$

The relative contact velocity vector, $\dot{\mathbf{r}}_C$, is defined in a similar way to Eq. (13), but the individual components correspond to the contact point i . The tangential constraint matrix \mathbf{W}_t is defined similarly, but with the tangential vector \mathbf{t}_i .

Like with Eq. (14), the vector of the relative contact velocities in the local normal-tangent coordinate system is

$$\dot{\mathbf{g}}_C = (\mathbf{W}_n \ \mathbf{W}_t) (\dot{\mathbf{q}}_C - \dot{\mathbf{q}}_S) + \dot{\mathbf{g}}_S, \tag{34}$$

where S and C denote the start and the end of the compression phase.

The motion Eq. (31) cannot be solved immediately, because neither the compression impulses $(\mathbf{I}_{nC} \ \mathbf{I}_{tC})^T$ nor the change of velocities during the compression $(\dot{\mathbf{q}}_C - \dot{\mathbf{q}}_S)$ are known. For the single contact of Section 3, the

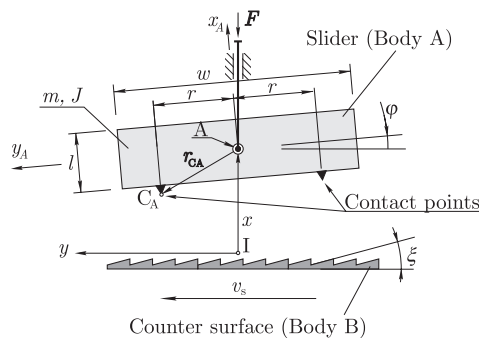


Fig. 3. 2-dof Model with two possible contact points and a counter surface with a sawtooth profile.

relative normal velocity during the compression can only diminish. In multiple concurrent contacts, interaction between the impulses can cause the relative normal velocities at some points to diminish, and at others to increase.

Physical consistency is ensured by applying complementarity conditions [34,35]. One complementarity condition is found for each contact in its normal direction. At the end of the compression, either the normal velocity is zero and the compression impulse is positive, or the normal velocity is positive and the compression impulse is zero, i.e., $\dot{g}_{nC,i} \geq 0$, $I_{nC,i} \geq 0$, and $\dot{g}_{nC,i} \cdot I_{nC,i} = 0$. The Coulomb friction limits the tangential compression impulse to $\mu \cdot I_{nC,i}$, if the relative velocity is non-zero at the end of the compression phase. Here, μ is the friction coefficient. The relative velocity is zero, if the tangential impulse is smaller than $\mu \cdot I_{nC,i}$. The complementarity conditions must comply with $|\dot{g}_{tC,i}| \geq 0$, $\mu I_{nC,i} - |I_{tC,i}| \geq 0$, and $|\dot{g}_{tC,i}| \cdot (\mu I_{nC,i} - |I_{tC,i}|) = 0$. Using the normal and tangential complementarity conditions, Eq. (31) is rewritten in the linear complementarity problem (LCP) form

$$\mathbf{y} = \mathbf{Ax} + \mathbf{b}, \tag{35}$$

$$\mathbf{y} \geq 0, \quad \mathbf{x} \geq 0, \quad \mathbf{y}^T \mathbf{x} = 0. \tag{36}$$

Pfeiffer and Glocker’s [35] straightforward formulation of the compression phase as an LCP has \mathbf{A} and \mathbf{b} known from the mass matrix, the active forces, and the contact kinematics. Complementary \mathbf{x} and \mathbf{y} , representing the unknown relative velocities and compression impulses, are normally found using *Lemke’s algorithm* [36].

4.1.2. Expansion phase

The conservation of momentum during the expansion phase gives

$$\mathbf{M}(\dot{\mathbf{q}}_E - \dot{\mathbf{q}}_C) - (\mathbf{W}_n \ \mathbf{W}_t) \begin{pmatrix} \mathbf{I}_{nE} \\ \mathbf{I}_{tE} \end{pmatrix} = \mathbf{0}. \tag{37}$$

The expansion impulse is the compression impulse multiplied by the coefficient of restitution. Interactions between multiple concurrent contacts can lead to physical inconsistency. An impulse at one contact point could force an interpenetration of surfaces at another contact point. To avoid this inconsistency, complementarity conditions must be introduced, and the expansion phase solved as an LCP [35].

Until impact, the motion equation (29) is integrated using the Runge–Kutta fourth-order method. During impacts, two LCPs are solved: the LCP for the compression phase, followed by the LCP for the expansion phase.

4.2. Numerical example: 1-contact model

For the comparison and verification we numerically simulated the one-contact, one-dof model of Section 2, with the parameter values given in Table 1. The bouncing ball has a radius of 1 μm . The counter-surface geometry has a sawtooth height of 1 μm and $\zeta = 4^\circ$. The maximum time-step, $\Delta t = 0.1 \mu\text{s}$, was made much shorter during the impacts to limit the interpenetration to $\delta = 0.01 \mu\text{m}$. With these values the analytical model

Table 1
Parameter values used in simulations

$m = 2 \times 10^{-5} \text{ kg}$	Slider mass
$w = 10 \text{ mm}$	Slider width (used in 2-contact model)
$k_l = 0.2$	l to w ratio (used in 2-contact model)
$k_r = 0.25$	r to w ratio (used in 2-contact model)
$v_s = 10 \text{ m/s}$	Sliding speed
$F = 2 \text{ N}$	Normal force
$\mu = 0.5$	Coefficient of friction (used in 2-contact model)
$\varepsilon_N = \varepsilon_T = \varepsilon = 0.5$	Coefficient of restitution
$\zeta = 4^\circ$	Sawtooth angle

of Section 2 gives $f_b = 11917.2$ Hz and $\dot{x}_E = 2.09780436$ m/s. With \dot{x}_E as the initial conditions for $\dot{x}(0)$ and $x(0) = 0$ m, the numerical simulations were stable with a frequency of 11917.1756 Hz and a post-impact velocity of 2.0978 m/s. The final (underlined> digit for the post-impact velocity alternated between 7 and 8 during the iterations. The numerical simulation results in Fig. 4 are similar to those in Fig. 1d.

4.3. Numerical example: 2-contact model

Added to the parameters of Table 1 are the normalized slider-height $k_l = 0.2$, the normalized radius of the contact point, $k_r = 0.25$, the coefficient of friction, $\mu = 0.5$, and the slider width, $w = 10$ mm. The counter-surface geometry had a sawtooth height of $4\ \mu\text{m}$ with $\xi = 4^\circ$, see Fig. 3. As shown in the results, later, the slider was bouncing several times higher than the sawtooth height. The total simulated time $T_{\text{sim}} = 0.01$ s. The two-contact solution in Section 3 gave $f_c = 20511.4$ Hz with the initial conditions $x(0) = 21.4\ \mu\text{m}$, $\varphi(0) = 8.6 \times 10^{-3}$ rad, $\dot{x}(0) = 1.22$ m/s, and $\dot{\varphi}(0) = -351.6$ rad/s. Because the left and right contacts are not symmetrical, the numerical results in Fig. 5 quickly diverge from the symmetrical closed-form solution of Section 3. Since the numerical simulation and the two-contact solution of Section 3 cannot be quantitatively compared, the spectral content of the waveforms was analyzed via a numerical Fourier transform, where $X(f)$ and $\dot{\Phi}(f)$ denote the Fourier transforms of x and $\dot{\varphi}(t)$, respectively. The velocities transformed more reliably than the displacements. In Fig. 6, the magnitude plots of \dot{X} and $\dot{\Phi}$ have distinct peaks at approximately 10.5 and 9.0 kHz, respectively. The frequency $f_c = 20511.4$ Hz of Eq. (28) differs from these numerically generated values, but actually represents the same periodic motion. The difference arises because the rectified sine wave

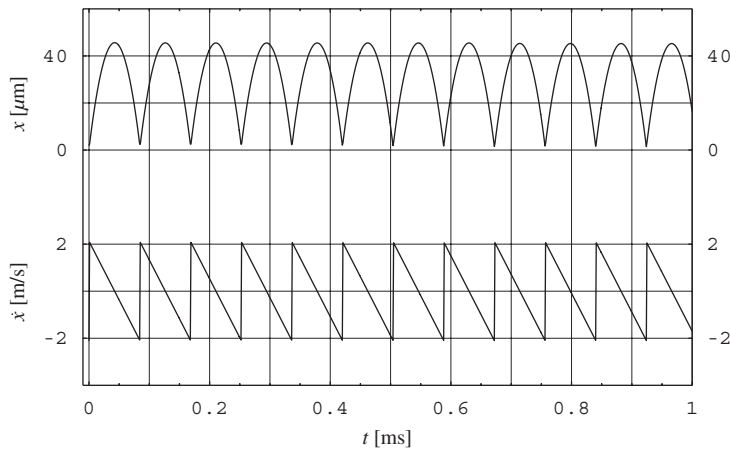


Fig. 4. Numerical simulation of ball bouncing.

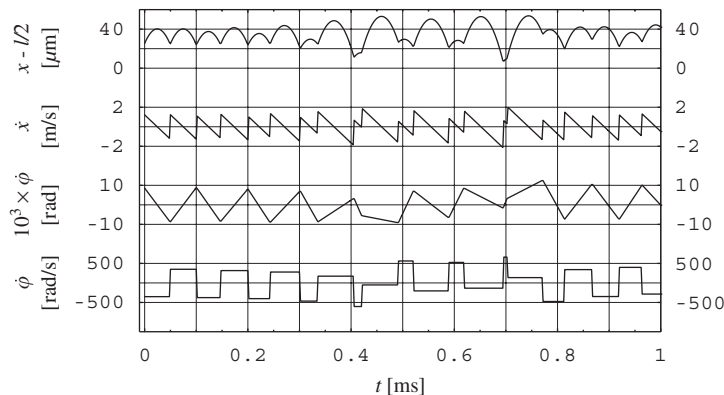


Fig. 5. Numerical simulation results of two-contact slider on sawtooth-shaped counter surface, with Table 1 parameter values.

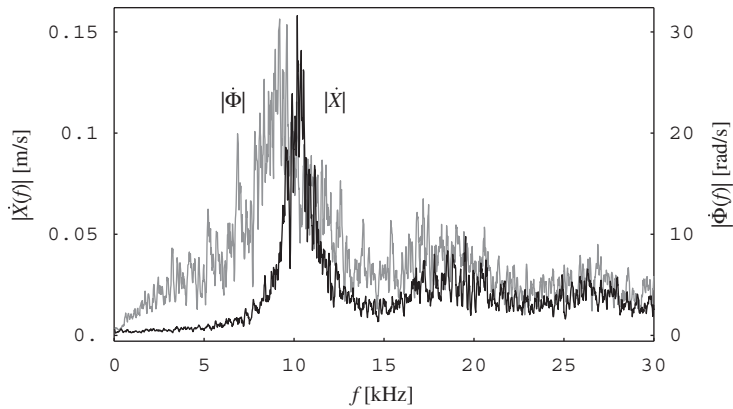


Fig. 6. Amplitude spectra $|\dot{X}|$ -black, and $|\dot{\Phi}|$ -gray.

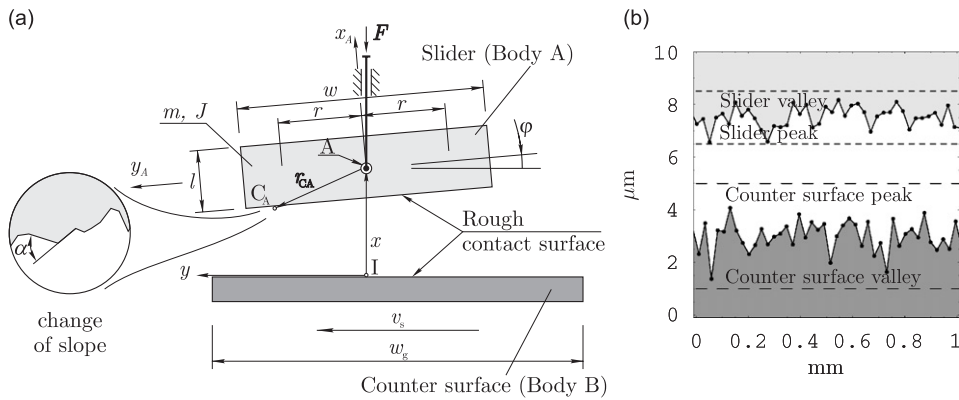


Fig. 7. (a) 2-dof Model with rough contact surfaces. (b) exaggerated example of rough contact surfaces, • contact points.

$|\sin(\omega t)|$ of the closed-form solution has its fundamental frequency at 2ω [37]. The first waveform of Fig. 5, a less than ideal rectified sine wave, has significant energy at the excitation frequency, ω . Consequently, the numerical algorithm identifies the measured frequency at

$$f_m = \frac{f_c}{2}, \tag{38}$$

where f_c is given by Eq. (28).

Increasing the friction coefficient beyond $\mu = 0.25$ moves the peak of $|\dot{\Phi}|$ to lower frequencies, while the frequency at which $|\dot{X}|$ peaks slightly increases. At $\mu = 0.5$ the peaks for $|\dot{X}|$ and $|\dot{\Phi}|$ are at 11.5 and 6 kHz, respectively. At $\mu = 1$ the peaks are at 12.0 and 3.5 kHz. During moderate friction (up to $\mu = 0.25$) the numerical simulation agrees well with the closed-form solution f_m for the slider mass m , the constant force F , the coefficient of restitution ε , the relative dimension k_l , and the velocity of sliding v_v . Regarding \dot{X} , the agreement is also good for higher levels of friction ($\mu \approx 0.5$). With k_l , the mass moment of inertia increases, and the non-symmetry becomes more pronounced. For $\mu > 0.5$ and $k_l > 0.5$, the slider becomes unstable and can rotate.

4.4. Numerical example: multiple-contacts between surfaces with random roughness

The two-contact numerical model of Section 4.3 was extended to a slider and a counter surface, both having random roughness with a defined peak-to-valley (a uniform peak-to-valley probability distribution was used), see Fig. 7. The fractal roughness models, first introduced by Ling [38], common in static contact problems,

were not considered. Here, the maximum vertical distance between any two contact points (shown as dots • in Fig. 7b) was limited by the maximum peak-to-valley via the maximum change of slope between two points. In accordance with the observation of Tabor [39] and Oden and Martins [2] the average change in the asperity slope was less than 15° . The slider had a width $w = 10$ mm and a peak-to-valley of $[-1, 1]$ μm . The contact shape was defined by 400 contact points, with $25 \mu\text{m}$ of distance between adjacent points (in the tangential direction, i.e., y_A in Fig. 7a). The counter surface had width $w_g = 0.22$ m, roughness range $[-2, 2]$ μm , and 10000 contact points with $22 \mu\text{m}$ between adjacent points. Fig. 8 is a typical histogram of the change of slope between the asperities, with standard deviations $\sigma_\alpha \approx 0.9^\circ$ and $\sigma_\beta \approx 1.3^\circ$, where α and β denote the slider and the counter surface, respectively.

A typical simulation result with the random roughness specified by Fig. 8 and the Table 1 parameter values is similar to the results in Fig. 5. These waveforms have the features of the counterparts in Figs. 1 and 4.

The discussion of the simulation results is continued after the wear phenomena have been introduced; however, due to the multiple concurrent contacts and the random nature of the rough surfaces, the system is highly nonlinear and non-smooth and, therefore, a periodic solution is, in general, not expected. This expectation results from Lorenz's classic work [40].

4.4.1. Run-in wear

A random surface roughness has very few asperities bearing the mechanical load. In a real slider, asperities bearing a high mechanical load deform or wear quickly, forcing other asperities to support the load. The effects of the wear will be included using Slavič and Boltežar's [33] surface-recession wear model. Here, the reduction in surface height

$$u_i = u_{\text{Max}} \frac{W_i}{W_{\text{Max}}} \quad (39)$$

at each contact point, i , depends on the total loss of mechanical energy at each contacting asperity, W_i , calculated from the contact impulses, \mathbf{I} , and the relative velocity, \mathbf{g} , after each cycle of duration T_{sim} . In Eq. (39) $W_{\text{Max}} = \text{Max}_i(W_i)$, and the maximum wear-particle size $u_{\text{Max}} = 2 \mu\text{m}$ keeps the roughness within the range of the initial contact shape.

This study considers the wear-in of the slider to conform to mechanical loads, see Figs. 9 and 10. Approximately 20 cycles of sliding (each of duration T_{sim}) achieved a steady-state contact shape, which resulted in a more homogenous distribution of the load. Conceptually, the energy-based wear law of Eq. (39) is consistent with Archard's wear law ($w = (k/H)(\mu Fl/\mu)$) [41], which contains the work μFl of sliding a distance l . The parameter of hardness, H , and the wear coefficient, k , are determined from experiments.

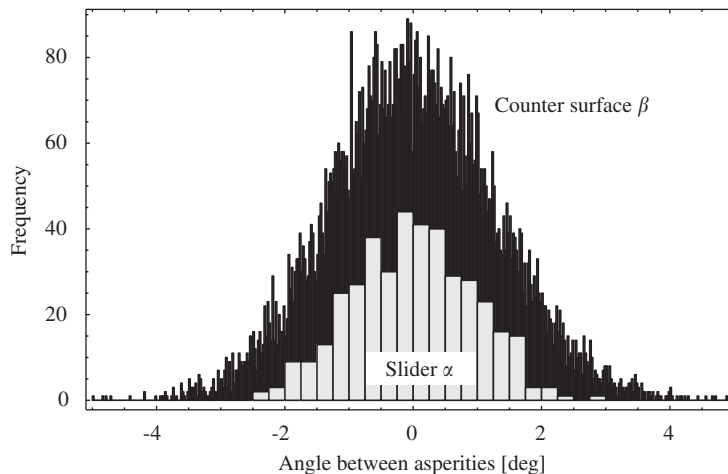


Fig. 8. Histogram of surface slope between asperities. Typical standard deviations: $\sigma_\alpha \approx 0.9^\circ$ and $\sigma_\beta \approx 1.3$.

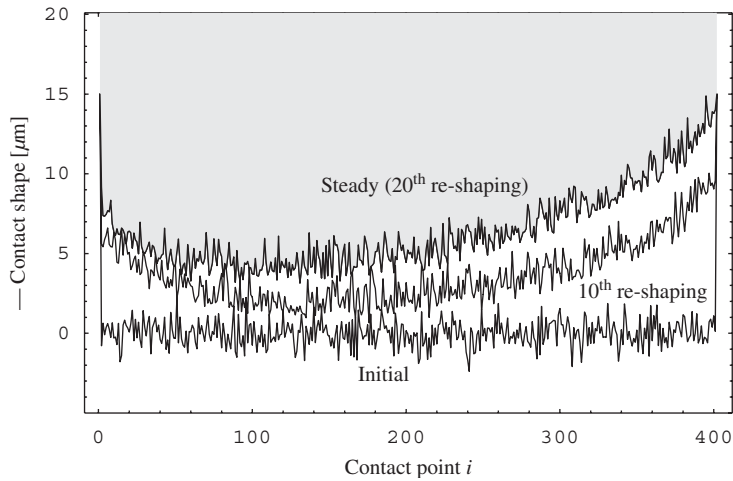


Fig. 9. Run-in wear of slider: change of slider's surface geometry.

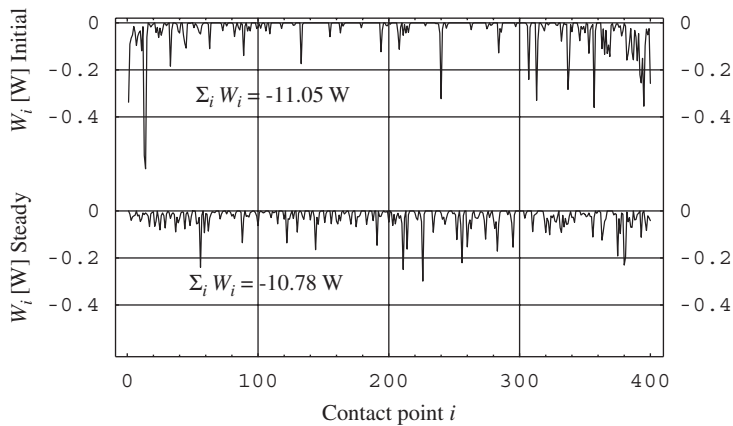


Fig. 10. Run-in wear of slider: loss of mechanical energy.

Curve fitting an arc to the contact shapes of Fig. 9 suggests the local radius of curvature reduces from a very large value to about 2–3 m. Fig. 10, which plots the energy losses, W_i , at the contact point i , suggests the edges of the slider ($i < 100$ and $i > 300$) are initially loaded more than average, while the middle is loaded less. After run-in wear, the load is more homogeneously distributed, which tends to maintain a steady-state contact shape.

4.4.2. Vibration frequency

Fig. 11 shows plots of the amplitude spectra of $|\dot{X}|$ and $|\dot{\Phi}|$ for the vibrations of a slider with its initial and steady-state contact shapes similar to Fig. 9, running against a rough counter surface. Fig. 11 is the result of 30 simulations, each with a different random-roughness combination. The shading bounds the data scatter over 30 simulations with one standard deviation. The means are indicated by solid curves.

For the initial contact shape (light shading and curve), the amplitude-spectrum $|\dot{X}|$ has a peak of 0.052 m/s at 10.3 kHz. For the steady-state shape (dark shading and curve), the peak rises to 0.065 m/s at 9.6 kHz, see Fig. 11a. Similarly, $|\dot{\Phi}|$ for the initial shape has a peak magnitude of 10.5 rad/s at 6.9 kHz. For the steady-state shape, the peak is 17.3 rad/s at 6.4 kHz, see Fig. 11b.

If a comparison is made, it is clear that the amplitude peak for $|\dot{X}|$ increases by approximately 25% from the initial to the steady state, and the center frequency slightly decreases. For $|\dot{\Phi}|$ the peak increases by approximately 65%, from the initial to the steady state, and the frequency is decreased slightly.

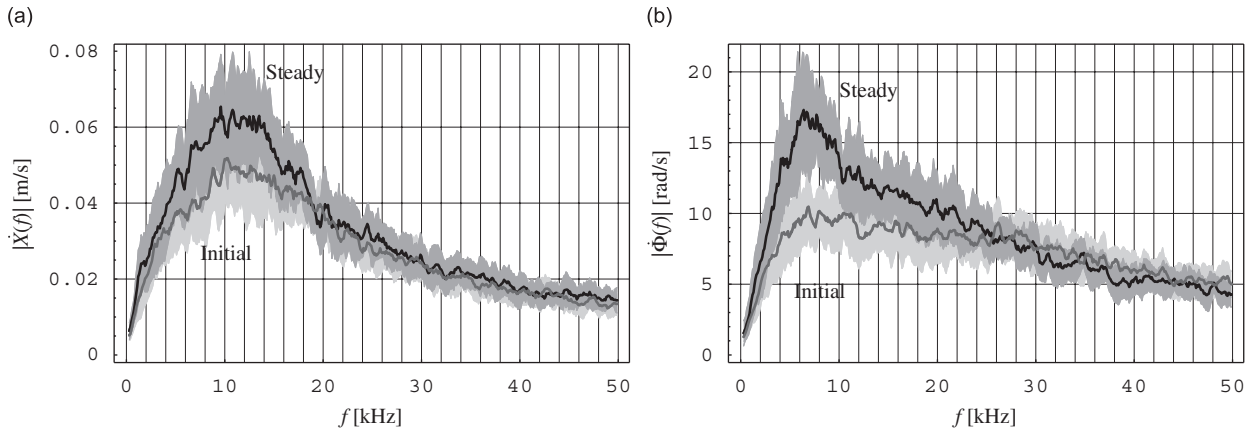


Fig. 11. Averaged amplitude spectra: (a) $|\dot{X}|$, (b) $|\dot{\Phi}|$. Light gray is used for the initial shape and dark for the steady-state shape. Shaded area denotes \pm standard deviation of averaged data.

The inclusion of wear changed the slider dynamics. Numerical simulations show that for the steady-state contact shape, the frequency peak becomes narrower and the amplitudes are higher. The effect of narrowing the frequency peaks is very obvious for the rotational degree of freedom $|\dot{\Phi}|$, which has a broad frequency content for the initial shape, see Fig. 11.

Similarly, as in Section 4.3, the frequency peaks for $|\dot{\Phi}|$ occurred at lower frequencies than for $|\dot{X}|$. With the friction coefficient the peaks of $|\dot{\Phi}|$ decreased and $|\dot{X}|$ slightly increased.

5. Comparison and discussion of the models

In Sections 2 and 4.2, we presented closed-form and numerical single-contact, single-dof models. Both gave bouncing motion resembling a rectified sine wave, at a frequency defined by Eq. (8). The numerical solutions matched the closed-form solutions. Both show that steady-state bouncing is possible on a sawtooth-shaped counter surface.

Table 2 compares the results for the bouncing frequency for $|\dot{X}|$, for the two-dof, two-contact closed-form solution of Section 3, the two-contact numerical model of Section 4.3, and the rough-surface numerical models of Section 4.4. The numerical simulations agree with the closed-form solution for most values of slider load, F , the slider mass, m , the sliding speed, v_s , the coefficient of restitution, ε , the shape parameter, k_l , and the roughness, see the middle of Table 2. For certain values of the coefficient of restitution (e.g., $\varepsilon = 0.25$), the numerical simulation gave lower (up to 20%) bouncing frequencies than the closed-form solution.

The numerical solution included friction (see the bottom of Table 2), which slightly increased the bouncing frequency of \dot{X} for most parameter values. However, friction in combination with thick sliders ($k_l > 0.5$) decreased the bouncing frequency of \dot{X} . The rocking frequency for $|\dot{\Phi}|$ is usually lower than the bouncing frequency for $|\dot{X}|$, and the difference increases with increasing friction.

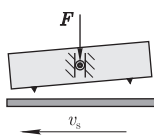
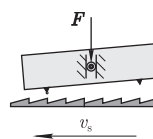
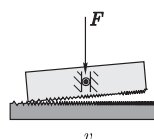
The closed-form solution included roughness effects via the sawtooth angle ξ . Random surface roughness is characterized by the standard deviation, σ , of the angle between the asperities shown in Fig. 8. For $\xi \approx 3\sigma$, similar bouncing frequencies were found for the sawtooth-shaped and random-roughness counter surfaces.

6. Experiment

6.1. Experiment setup and discussion of the results

To verify the solutions generated in Sections 2–4, bouncing-slider tests were performed using the setup shown in Fig. 12. The vertical motion was measured by an ADE MicroSense 3046 capacitance gauge system (range $\pm 50 \mu\text{m}$, resolution $1 \mu\text{m}$, bandwidth 40 kHz).

Table 2
Comparison of models for parameters given in Table 1

	 Closed-Form (38)	 Numeric	 Numeric
Contacts between bodies	2	2	Multiple
Phenomena included	F, m, v_s, ϵ, k_l	$F, m, v_s, \epsilon, k_l, \mu$	$F, m, v_s, \epsilon, k_l, \mu$
Roughness	Idealized vert.	Sawtooth	Random surface
Via	Velocity	ξ	With wear
Parameters	\dot{X} frequency peak for $\mu = 0$ (kHz)		
	10.3	10.5	10.3
$v_s/2$ or $m/2$ or $2F$	20.5	21–22	20–22
$2v_s$ or $2m$ or $F/2$	5.1	5	5–6
$k_l = 0.5$	9.5	9	8
$\epsilon = 0.20$	23.8	21.0	19–21
$\epsilon = 0.25$	18.5	18.5	14
$\xi = 2^\circ$	23.8	20.0	
S: $[-0.5, 0.5] \mu\text{m}$, CS: $[-1, 1] \mu\text{m}$			20
Parameters	\dot{X} frequency peak for $\mu = 0.5$ (kHz)		
	–	12	10.5
$v_s/2$ or $m/2$ or $2F$	–	23	20–25
$2v_s$ or $2m$ or $F/2$	–	6	5–6
$k_l = 0.5$	–	12	7
$\epsilon = 0.25$	–	21	13

Steady-state results are given for the rough surface model. Left column denotes which of the common parameters. S—Slider, CS—Counter Surface.

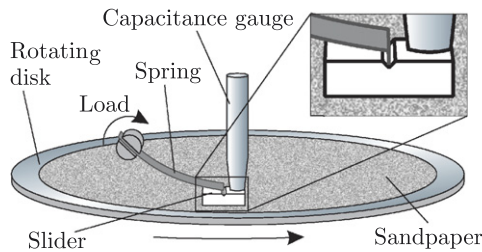


Fig. 12. Experimental setup.

A steel slider of mass $m = 2 \text{ g}$ with low magnetic permeability ran against a rotating disk extracted from a personal computer hard drive (Conner 3600 rev/min and Maxtor 5400 rev/min were used). The slider width was $w = 10.9 \text{ mm}$ with a height, l , ratio corresponding to $k_l = l/w = 0.2$. The load was applied by a 20 mm × 10 mm torsional spring made of thin aluminum sheet. When the spring-mass system was not in contact with the disk, its natural frequency was approximately 40 Hz; however, sliding against a surface sanded with SP600 and then polished to a mirror-like surface, initially resulted in a broad amplitude spectra, without distinct frequency peaks. The natural frequencies of the system at rest (no sliding), measured from the slider, were not affected by the slider load.

Sandpaper (SP) sheets of 220, 400, and 600 grit were affixed to the rotating base, to impose roughness and accelerate run-in wear. Upon initial contact, the surface oscillations were broad-band and/or totally random and hard to reproduce. After run-in wear re-shaped the contact surface, distinct vibrations were observed. As in the numerical simulations of Section 4.4.4, the sliders edges wore more.

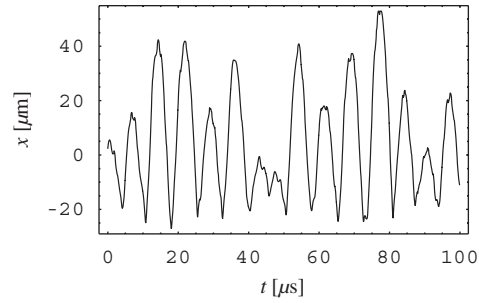


Fig. 13. Typical displacements measured at 16 m/s sliding speed on SP400.

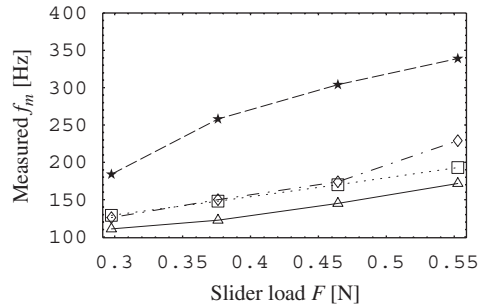


Fig. 14. Measured frequencies versus slider load sliding at 16 m/s on \triangle SP 220, \square SP 400, \diamond SP 400, \star sanded with SP400.

Typical measured displacements for a slider running against SP400 at sliding speed $v_s = 16$ m/s, and load $F \approx 0.45$ N are plotted versus time in Fig. 13. A Fourier transform of the waveform exhibited a clear peak at 145 Hz. The measured displacement in Fig. 13 is similar to that predicted in Figs. 1, 4, and 5.

For a comparison of the experimentally measured frequency of the roughness-induced vibration with the closed-form analytical model (38) is used

$$f_m = \frac{1}{2} \frac{F}{2mv_s \tan \xi} \frac{1 - \varepsilon}{1 + \varepsilon} \frac{1 + k_l^2 + 12k_r^2}{1 + k_l^2}. \quad (40)$$

The analytically deduced frequency of the roughness-induced vibration involves roughness (via the sawtooth angle, ξ), the slider load, F , the slider mass, m , the coefficient of restitution, ε , the sliding speed v_s , the slider height-to-width ratio $k_l = l/w$, and $k_r = r/w$; however, there was no coefficient of friction. For the experimental slider all parameters except those for ε and ξ are known. At room temperature for metal-on-metal impacts, the coefficient of restitution ε can be estimated as 0.6–0.8. However, since during the experiment the slider became too hot to touch (temperatures probably exceeded 60 °C) and because at the contact spots temperatures should be much higher, the effect of temperature on the impact is expected to be significant. As the contact-spot temperature is nearly impossible to measure we estimated that the coefficient of restitution is small (≈ 0.1). Using $\varepsilon = 0.1$, with a reasonable roughness parameter of $\xi = 2^\circ$, Eq. (40) gives $f_m = 142$ Hz. By making the reasonable assumption of two parameters (ε, ξ) the analytical model gives good results.

Eq. (40) suggests the slider load, F , increases the vibration frequency. Experimentally, this was verified for different sliding conditions: fresh SP600, SP400, SP220, and a metal disk surface roughened with SP400,¹ see Fig. 14, where the measured frequency, f_m , versus slider load, F , is shown. As predicted by Eq. (40), the experiments showed a linear increase of the frequency with load.

¹For metal-on-metal tests, slider wear-in was done by running against sandpaper, and then running the pre-worn slider against the metal disk.

Furthermore, Eq. (40) suggests that the increased roughness—described by parameter ξ —decreases the frequency of vibration. Experimentally, we found the amplitude spectral peaks for the smoother SP had a wider bandwidth than the rougher SP, although the spectral peaks occurred at comparable frequencies. As expected, the metal slider running against the SP400-roughened metal disk produced higher frequencies of vibration than when running on sandpaper. The frequencies could differ due to the smaller asperity angles of the metal-on-metal contact or due to the lower stiffness of the sandpaper grains fixed to the paper backing. A wear-track pattern formed on the rotating surface. Sliding against a surface sanded with SP600 and then polished to a mirror-like surface, initially resulted in a broad amplitude spectrum, without distinct frequency peaks. However, after 30–50 m of sliding, the mirror-like surface roughened, leading to results similar to the disk surface roughened by sandpaper with SP400. The wear of the SP increased the frequency.

Furthermore, Eq. (40) suggests an increased sliding speed, v_s , would linearly decrease the frequency of vibration. Fig. 15 plots the measured frequency, f_m , versus the sliding speed, v_s , for sliding on SP400. As predicted by the model, in the experiment, f_m decreases approximately linearly with the sliding speed, v_s .

The experiment showed that the thicker sliders (higher $k_l = l/w$ ratio) were more unstable, and were prone to rotate.

Occasionally, the measured displacements contained multiple harmonics associated with the spindle's rotation frequency. As predicted by Eq. (40), and verified by experiment, the roughness-induced vibration frequency decreases during the acceleration of the spindle. At the same time, the frequency of the harmonics increases. These observations clearly distinguished the roughness-induced vibrations from the harmonics.

6.2. Comparison with published experiments

By focusing on the roughness-induced vibration the models avoided the stiffness and damping elements. Since this situation is usually not appropriate for real-life applications, Eq. (40) cannot be applied directly. However, since the source of the vibrations is the same, a qualitative agreement can be expected.

Best et al. [42] and later Suk et al. [43] studied the effects of disk roughness on air-bearing sliders. For vibrations normal to the disk surface they measured an increase of the oscillating frequency as the sliding velocities decreased. At low sliding velocities (pre-flying speed), increased roughness (i.e., the sawtooth angle ξ) increased the flying height. These observations are consistent with Eq. (40). At low sliding speeds Best et al. found the roughness increased the oscillating frequency, but Suk et al. found the roughness to be insignificant. According to Eq. (40), roughness should decrease the oscillating frequency.

Ono and Takahashi [44] studied the bouncing vibrations of a slider on a wavy disk surface. A single-dof elastic-contact model gave results almost the same as a single-dof collision-contact model. Ono and Takahashi's collision model is similar to that presented in Section 2. For a single contact, single-dof slider on a random rough surface, Ono and Iida [22] studied the bouncing frequencies and related the roughness to bounce-free sliding and low wear. Their numerical simulations agree with the closed-form solution of Eq. (40). A higher slider load (i.e., force F), a smaller slider mass (i.e., m), a higher contact damping (i.e., a smaller coefficient involving restitution ϵ), and a smoother disk (i.e., a smaller sawtooth angle ξ) increased the critical

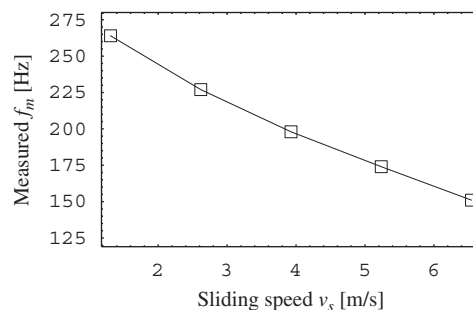


Fig. 15. Measured frequency versus sliding speed at SP400 for load $F = 0.45$ N.

frequency. Ono and Iida's [22] experiment of a spherical glass slider running against a rotating hard disk qualitatively agrees with their numerical model.

Fig. 10 of Ono and Iida [22] measures the effects of the applied slider load on the vibration frequency. As predicted by Eq. (40), the frequency was found to be linearly related to the slider load [22].

Slider dynamics has been applied to brakes. Due to the interaction of two flexible bodies, the contact-induced vibrations are usually found close to the natural frequencies of the coupled system. Giannini et al. [45] attributed their measured linear increase of squeal noise with a normal load to a higher contact stiffness. Eq. (40) gives an alternative explanation, with a more direct influence of the force. Furthermore, as predicted here, Giannini et al. experimentally observed that the wear increases the squeal noise. By decreasing the angle of attack (which can be explained by the angle φ_E , Eq. (22)) they measured a higher frequency of squeal. Giannini et al. experimentally show both the in-plane (tangential) and the out-of-plane (normal) pad dynamics during the squeal to be sinusoidal. They found the phase difference between the sinusoids to be 90° . We view this as evidence that the full-body motion studied here influences the squeal. As predicted by Eq. (40), Giannini et al. found the sliding speed increased the vibration amplitudes (i.e., the sliding speed, v_s).

7. Summary and conclusions

We studied roughness-induced vibrations using theory and experiment. Usually, roughness effects are included via different variations of the friction law, which can result in distinct vibrations. Frequently, the studied stiffness effects of the slider system can also result in distinct vibrations. By using Poisson's impact law and Coulomb's friction law on geometrically detailed contact surfaces of rigid bodies, roughness effects were directly included into a closed-form solution resulting in distinct vibrations. This finding is quite surprising. Also, experimentally in this article we found that the sliding of bodies with a random roughness leads to distinct vibrations that increase with wear.

Closed-form and numerical solutions, including Eq. (41) below, agree with the experiments.

From our study we can conclude that:

- (1) Random roughness can induce vibrations with distinct and predictable center frequencies.
- (2) The wear-in of a slider narrows the amplitude spectral peaks and increases the peak height.
- (3) The frequency of the vibrations induced by a slider sliding on an idealized sawtoothed surface, Eq. (40),

$$f_m = \frac{1}{2} \frac{F}{2mv_s \tan \xi} \frac{1 - \varepsilon}{1 + \varepsilon} \frac{1 + k_l^2 + 12k_r^2}{1 + k_l^2} \quad (41)$$

involves roughness (via the sawtooth angle, ξ), the slider load, F , the slider mass, m , the coefficient of restitution, ε , the sliding speed, v_s , the slider height-to-width ratio, $k_l = l/w$, and $k_r = r/w$. The width, w , of the slider has no direct influence.

- (4) The phenomena observed on hard-disk drives [22] and car brakes [45] could be explained by the theory presented in this article.
- (5) The amplitudes of the roughness-induced vibrations decrease with high slider loads or a small slider mass. The center frequency of the amplitude spectra peak increases.
- (6) Roughness-induced vibrations can be important when the bouncing amplitude is several times higher than the roughness heights.

Possible applications include the following: hard-disk drives, millimeter- and micrometer-sized micro-electro-mechanical systems (MEMS), and brakes at low braking force. Especially for small systems the surfaces and defects are pronounced, and the roughness could induce vibrations [46,47].

Acknowledgments

The support provided to the first author by the US Government in the form of a Fulbright Fellowship (Grant ID: 15054674) is deeply appreciated. The hospitality of the Mechanical Engineering Department at University of Texas at Austin is also gratefully acknowledged.

References

- [1] S. Antoniou, A. Cameron, C. Gentle, The friction-speed relation from stick–slip data, *Wear* 36 (1976) 235–254.
- [2] J. Oden, J. Martins, Models and computational methods for dynamic friction phenomena, *Computer Methods in Applied Mechanics and Engineering* 52 (1–3) (1985) 527–634.
- [3] J. Martins, J. Oden, F. Simoes, Recent advances in engineering science—a study of static and kinetic friction, *International Journal of Engineering Science* 28 (1) (1990) 29–92.
- [4] D. Crolla, A. Lang, Brake noise and vibration—state of art, *Tribologie* 18 (1991) 165–174
D. Crolla, A. Lang, *Vehicle Tribology*, Elsevier, Amsterdam.
- [5] R. Ibrahim, Friction-induced vibration, chatter squeal and chaos. Part I: mechanics of friction, part II: dynamics and modeling, in: R. Ibrahim, A. Soom (Eds.), *Friction-Induced Vibration, Chatter Squeal and Chaos*, Vol. 49, *ASME Winter Annual Meeting*, Anaheim, DE, 1992, pp. 107–138.
- [6] I. Grabec, Chaotic dynamics of the cutting process, *International Journal of Machine Tools & Manufacture* 28 (1) (1988) 19–32.
- [7] K. Popp, P. Stelter, Stick–slip vibrations and chaos, *Philosophical Transactions of the Royal Society of London Series A—Mathematical Physical and Engineering Sciences* 332 (1624) (1990) 89–105.
- [8] G. Whiston, Impacting under harmonic excitation, *Journal of Sound and Vibration* 67 (2) (1979) 179–186.
- [9] S. Shaw, P. Holmes, A periodically forced piecewise linear-oscillator, *Journal of Sound and Vibration* 90 (1) (1983) 129–155.
- [10] A. Nordmark, Nonperiodic motion caused by grazing—incidence in an impact oscillator, *Journal of Sound and Vibration* 145 (2) (1991) 279–297.
- [11] S. Foale, S. Bishop, Dynamical complexities of forced impacting systems, *Philosophical Transactions of the Royal Society of London Series A—Mathematical Physical and Engineering Sciences* 338 (1651) (1992) 547–556 (Nonlinear Dynamics of Engineering Systems).
- [12] N. Hinrichs, M. Oestreich, K. Popp, Dynamics of oscillators with impact and friction, *Chaos, Solitons & Fractals* 8 (4) (1997) 535–558.
- [13] F. Pfeiffer, A. Kunert, Rattling models from deterministic to stochastic processes, *Nonlinear Dynamics* 1 (1990) 63–74.
- [14] S. Bishop, Impact Oscillators, *Philosophical Transactions of the Royal Society of London Series A—Mathematical Physical and Engineering Sciences* 347 (1683) (1994) 347–351 (Impact Oscillators).
- [15] H. Cho, J. Barber, Stability of the three-dimensional coulomb friction law, *Proceedings of the Royal Society of London Series A—Mathematical, Physical and Engineering Sciences* 455 (1983) (1999) 839–861.
- [16] N. Kinkaid, O. O'Reilly, P. Papadopoulos, On the transient dynamics of a multi-degree-of-freedom friction oscillator: a new mechanism for disc brake noise, *Journal of Sound and Vibration* 287 (4–5) (2005) 901–917.
- [17] U. Andreaus, P. Casini, Dynamics of friction oscillators excited by a moving base and/or driving force, *Journal of Sound and Vibration* 245 (4) (2001) 685–699.
- [18] A. McMillan, A non-linear friction model for self-excited vibrations, *Journal of Sound and Vibration* 205 (3) (1997) 323–335.
- [19] P. Vielsack, Stick–slip instability of decelerative sliding, *International Journal of Non-linear Mechanics* 36 (2) (2001) 237–247.
- [20] J. Ogilvy, Numerical-simulation of friction between contacting rough surfaces, *Journal of Physics D—Applied Physics* 24 (11) (1991) 2098–2109.
- [21] M. Bengisu, A. Akay, Relation of dry-friction to surface roughness, *Journal of Tribology—Transactions of the ASME* 119 (1) (1997) 18–25.
- [22] K. Ono, K. Iida, Statistical analysis of perfect contact and wear durability conditions of a single-degree-of-freedom contact slider, *Journal of Tribology—Transactions of the ASME* 122 (1) (2000) 238–245.
- [23] W. Chang, F. Ling, Normal impact model of rough surfaces, *Journal of Tribology—Transactions of the ASME* 114 (3) (1992) 439–447.
- [24] H. Ouyang, J. Mottershead, M. Cartmell, D. Brookfield, Friction-induced vibration of an elastic slider on a vibrating disc, *International Journal of Mechanical Sciences* 41 (3) (1999) 325–336.
- [25] T. Richard, E. Detournay, Stick–slip motion in a friction oscillator with normal and tangential mode coupling, *Comptes Rendus de la Academie des Sciences Paris, Serie Iib* 328 (2000) 671–678.
- [26] J. Mottershead, H. Ouyang, M. Cartmell, M. Friswell, Parametric resonances in an annular disc, with a rotating system of distributed mass and elasticity; and the effects of friction and damping, *Proceedings of the Royal Society of London Series A—Mathematical, Physical and Engineering Sciences* 453 (1956) (1997) 1–19.
- [27] L. Wood, K. Byrne, Analysis of a random repeated impact process, *Journal of Sound and Vibration* 78 (3) (1981) 329–345.
- [28] P. Holmes, The dynamics of repeated impacts with a sinusoidally vibrating table, *Journal of Sound and Vibration* 84 (2) (1982) 173–189.
- [29] C. Budd, F. Dux, A. Cliffe, The effect of frequency and clearance variations on single-degree-of-freedom impact oscillators, *Journal of Sound and Vibration* 184 (3) (1995) 475–502.
- [30] S. Poisson, *Traité de Mécanique*, Bachelier, Paris.
- [31] J. Slavič, M. Boltežar, Nonlinearity and non-smoothness in multibody dynamics: application to woodpecker toy, *Journal of Mechanical Engineering Science* 220 (3) (2006) 285–296.
- [32] J. Slavič, Nonlinear and Nonsmooth Dynamics of Discretely Defined System of Rigid Bodies with Unilateral Contacts, PhD Thesis, Faculty of Mechanical Engineering, University of Ljubljana, 2005.
- [33] J. Slavič, M. Boltežar, Simulating multibody dynamics with rough contact surfaces and run-in wear, *Nonlinear Dynamics* 45 (3–4) (2006) 353–365.

- [34] P. Lötstedt, Coulomb friction in two-dimensional rigid body systems, *Zeitschrift für Angewandte Mathematik und Mechanik* 61 (1981) 605–615.
- [35] F. Pfeiffer, C. Glocker, *Multibody Dynamics with Unilateral Contacts*, Wiley, New York, 1996.
- [36] R. Cottle, G. Dantzig, Complementary pivot theory of mathematical programming, *Linear Algebra and its Applications* 1 (1968) 103–125.
- [37] E. Angelo, *Electronics: BJTs, FETs, and Microcircuits*, McGraw-Hill, New York, NY, 1969.
- [38] F. Ling, Fractals, engineering surfaces and tribology, *Wear* 136 (1) (1990) 141–156.
- [39] D. Tabor, Friction—the present state of our understanding, *Journal of Lubrication Technology—Transactions of the ASME* 103 (2) (1981) 169–179.
- [40] E. Lorenz, Deterministic nonperiodic flow, *Journal of the Atmospheric Sciences* 20 (1963) 130–141.
- [41] J. Archard, Contacts and rubbing of flat surfaces, *Journal of Applied Physics* 24 (1953) 981.
- [42] G. Best, K. Deckert, S. Millman, G. Singh, Effect of disk roughness on slider dynamics, *IEEE Transactions on Magnetics* 24 (6) (1988) 2748–2750.
- [43] M. Suk, B. Bhushan, D. Bogy, Role of disk surface-roughness on slider flying height and air-bearing frequency, *IEEE Transactions on Magnetics* 26 (5) (1990) 2493–2495.
- [44] K. Ono, K. Takahashi, Bouncing vibration and complete tracking conditions of a contact recording slider model on a harmonic wavy disk surface, *Journal of Tribology—Transactions of the ASME* 119 (4) (1997) 720–725.
- [45] O. Giannini, A. Akay, F. Massi, Experimental analysis of brake squeal noise on a laboratory brake setup, *Journal of Sound and Vibration* 292 (1–2) (2006) 1–20.
- [46] R. Rudd, J. Broughton, Coupling of length scales and atomistic simulation of a mems device, *International Conference on Modeling and Simulation of Microsystems*, SFA, Inc., USA, 1998, pp. 287–291.
- [47] X. Zhao, H. Dankowicz, C. Reddy, A. Nayfeh, Modeling and simulation methodology for impact microactuators, *Journal of Micromechanics and Microengineering* 14 (6) (2004) 775–784.